Understanding the Origin of Higher Capacity for Ni-Based Disordered Rock-Salt Cathodes

Musa Ali Cambaz, Alexander Urban, Syed Atif Pervez, Holger Geßwein, Alexander Schiele, Alexander A. Guda, Aram L. Bugaev, Andrey Mazilkin, Thomas Diemant, R. Jürgen Behm, Torsten Brezesinski, and Maximilian Fichtner*

ABSTRACT: Lithium excess disordered rock salt oxides have opened up a new vista in search of high capacity cathodes, resulting in a variety of new materials with versatile elemental compositions. This work introduces W^{6+} as a possible charge compensator and explores the solid solution series $Li_{1+x/100}Ni_{1/2-x/120}Ti_{1/2-x/120}W_{x/150}O_2$ (x = 0, 5, 10, 15, 20), which has been rationally developed based on concepts from percolation theory. Consistent with this understanding, the specific capacities increase from stoichiometric toward lithium excessive compositions, while simultaneously capacity retention decreases considerably. Specifically, $Li_{1.2}Ni_{1/3}Ti_{1/3}W_{2/15}O_2$ exhibits a first charge capacity of 246 mAh g^{-1}, which exceeds the theoretical transition metal redox capacity. To understand this peculiarity, we characterize the redox mechanism of nickel, titanium, tungsten, and oxygen using X ray absorption spectroscopy, X ray photoelectron spectroscopy, density functional theory calculations, and differential electrochemical mass spectrometry. We demonstrate that oxygen evolution takes place for $Li_{1.2}Ni_{1/3}Ti_{1/3}W_{2/15}O_2$ predominantly above 4.4 V vs Li^+/Li but was absent for the stoichiometric $LiNi_{0.5}Ti_{0.5}O_2$. The oxygen oxidation causes instability of the anion framework, resulting in oxygen loss, which incurs severe capacity fading and leads to the observed voltage hysteresis. These findings provide important implications for the development and design of novel high capacity lithium excess nickel based cathode materials.

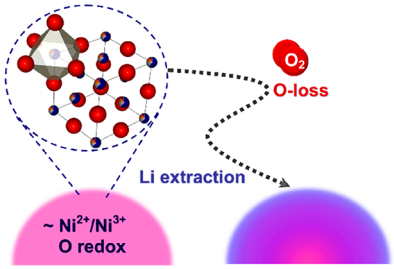

INTRODUCTION

Recent developments in the automotive and grid energy storage raise the question of whether the supply can meet the demand of the critical constituents for the future. Especially cobalt, which is still an essential component of the modern day battery, is argued to be the more critical element in terms of sufficient availability.[1] Therefore, research into the development of cobalt free alternative materials is required for next generation Li ion batteries. The implications for research have been a continuous decrease in the cobalt content toward more nickel [2,3] and manganese rich[4] compounds. Hence, the development of low cost and well performing positive electrode materials is clearly necessary.

Currently, rock salt related complex oxides like the derivatives of layered $LiCoO_2$[5,6] and spinel like $LiMn_2O_4$[7,8] and polyanionic compounds like $LiFePO_4$[9] are considered state of the art. The former is preferred in automotive and portable applications due to the high energy density. As a potential alternative, rock salt related oxides display a variety of lattice structures with ordered and disordered structures. In ordered structures, different cation ordering arrangements are possible with Li sites (sublattice) percolating over the entire structure.[10] The disordered structures cover a broader range from partially disordered, due to antisite defects[11,12] and/or cation migration,[13,14] to the fully cation disordered material with Li and transition metals sharing the same site statistically. A typical representative for the latter is the cubic α $LiFeO_2$.[15] Until recently, the design space for the development of "ordered" positive electrode material has been limited to transition metals that show minor or no intermixing of cations between the transition metal and lithium sublattices, as this is regarded being the prerequisite for good performance and stability. To meet these stringent requirements, only a few systems with specific chemistries (cobalt containing for rock salt oxides) have so far been able to perform sufficiently.[5] In general, local structural disorder, stemming from the statistical distribution of different cations at the same crystallographic site, has been regarded to adversely affect the overall lithium diffusivity and therefore to limit the electrode performance. This has inevitably ruled out several classes of materials. One of these are disordered rock salt oxides adopting cubic α $LiFeO_2$ type[16] structures, where Li and transition metals share the same cation site with a random distribution and no long range order.

As a result, these materials have not been paid attention to for a long time, as their performance is not comparable to that of modern materials. Especially micron sized, well crystalline particles show relatively poor electrochemical activity.[17] However, recent findings have shown that this may not necessarily be the case in general;[18,19] several new Li rich compositions capable of inserting/extracting a reasonable amount of lithium have been demonstrated. Albeit cation disorder is expected to be detrimental to the battery performance, at an excess of at least 10% lithium, diffusion can become facile, unveiling the hidden potential of Li rich disordered rock salt structures.[20−23] Without the requirement to be "well layered" as described above, new chemistries/substitutions can be explored, which may pave the way for the development of cobalt free materials. However, a significant fraction of the charge originates from reversible oxygen redox (rather than mainly oxygen release).[20,21] Unfortunately, the gain in capacity is associated with a number of problems such as sensitivity to the processing conditions, voltage hysteresis, transition metal migration, surface disorder, and the irreversible release of lattice oxygen as major roadblocks toward the realization of stable disordered rock salt materials.[24]

A widely used approach for the design of new lithium rich compositions comprises the hypothetical solid solution between a stoichiometric disordered rock salt and a lithium enriched phase with predominantly d^0 cations. Note that the latter has been shown to favor the stabilization of the disordered phase.[25] Alternatively, disorder can be induced by (de)lithiation,[26] and/or disordered phases can be formed directly by high energy milling. Because d^0 cations are not expected to undergo a redox reaction in the pristine state (fully lithiated), cations with high oxidation number are particularly attractive, given that more equivalents of lithium can be introduced for the reason of charge balancing and less compromise needs to be made on the side of the substituted redox active transition metal. Following this idea, chemistries/substitutions with V^{+4},[27,28] Ti^{4+},[29,30] Sb^{5+},[31] Nb^{5+},[20] Ta^{5+},[32] and Mo^{6+}[33,34] have been explored, leading to a considerable diversity of candidates for new cathode materials.

Several Ni based disordered rock salts have been reported up to now with different compositions, containing Ni^{2+}−Ti−Mo,[24,33] Ni^{2+}−Ta,[35] Ni^{2+}−Nb,[20] Ni^{2+}−Ti−Nb,[36,37] Ni^{2+}−Zr,[27] Ni^{2+}−V,[27] and Ni^{2+}−Ti.[38,39] The theoretical $Ni^{2+/4+}$ redox couple, which promises higher operating voltages, makes Ni based compounds attractive for application in positive electrode materials. However, X ray absorption spectroscopy (XAS) studies on $Li_{1.2}Ni_{0.333}Ti_{0.333}Mo_{0.133}O_2$,[24,33] $Li_{1.3}Ni_{0.27}Ta_{0.43}O_2$,[35] and $Li_{1.2}Ni_{0.35}Ti_{0.35}Nb_{0.1}O_{1.8}F_{0.2}$[40] suggest incomplete utilization of the Ni redox reservoir in most of these compounds, with Ni^{2+} being oxidized roughly to Ni^{3+} during charging and competing with O oxidation. This observation is also in agreement with theoretical predictions that $Ni^{3+/4+}$ redox occurs at higher voltages in disordered rock salts.[62]

In this work, we investigate a new family of Li rich disordered rock salt oxides, namely, $Li_{1+x/100}Ni_{1/2-x/120}Ti_{1/2-x/120}W_{x/150}O_2$ (x = 0, 5, 10, 15, 20), which have been rationally designed applying concepts of percolation theory. We show the feasibility of W^{6+} as a high valence cation to increase the Li content in disordered rock salts. Using a combination of diffraction and spectroscopic techniques and density functional theory (DFT) calculation, the role of Ni, W, and O in the charge compensation during electrochemical (de)lithiation was elucidated. The $Li_{1.2}Ni_{0.333}Ti_{0.333}W_{0.133}O_2$ (x = 20) phase delivers a large reversible specific capacity beyond the $Ni^{2+/4+}$ redox couple (only 60% accessible predicted by DFT), which suggests that half of the capacity should be due to anion redox during the first charge. We also demonstrate by differential electrochemical mass spectrometry (DEMS) that lithium excess invokes oxygen redox and triggers oxygen evolution, accompanied by a large voltage hysteresis. X ray photoelectron spectroscopy (XPS) analysis of the cathode materials showed no change in the oxidation state of Ti and W after oxygen loss. Structural changes were probed by *in situ* X ray diffraction (XRD) and extended X ray absorption fine structure (EXAFS), indicating irreversible changes after oxygen loss. Finally, the phenomena of oxygen loss and voltage hysteresis, often observed for Ni based disordered rock salts, are being discussed.

RESULT AND DISCUSSION

Synthesis and Characterization. We chose to investigate the solid solutions of the stoichiometric disordered *Fm*3*m* Li_2NiTiO_4 ($LiNi_{0.5}Ti_{0.5}O_2$) and the lithium rich cation ordered (*P*1) Li_4WO_5 ($Li_{1.6}W_{0.4}O_2$), targeting lithium rich disordered Li−Ni−Ti−W oxides. $LiNi_{0.5}Ti_{0.5}O_2$ adopts an α $LiFeO_2$ type crystal structure without long range cation order. Li and transition metals are randomly distributed over the octahedral sites. These types of compounds are referred to as disordered rock salt oxides. In the cation ordered triclinic *P*1 Li_4MO_5, with M = W^{6+} and Mo^{6+}, the latter cations occupy octahedral sites in a cubic close packed (ccp) anion sublattice, with the lithium ions residing on the remaining octahedral sites. Edge sharing MO_6 octahedra form a $[M_2O_{10}]$ unit in the ccp lattice.[41,42] A series of compounds with gradual increase in Li excess level was targeted, the compositions of which are given in Table 1. Hereafter, $LiNi_{0.5}Ti_{0.5}O_2$ is referred to as LNT 0 and the solid solutions as LNTW X, with X being the targeted lithium excess value.

Table 1. Targeted vs Measured Li/Ni/Ti/W Atomic Ratio for All Compounds from ICP OES

materials	Li excess/%	targeted ratio	measured ratio
LNT-0	0	1.00:0.50:0.50:0	0.99:0.51:0.50:0
LNTW-5	5	1.05:0.46:0.46:0.03	1.06:0.46:0.47:0.04
LNTW-10	10	1.10:0.42:0.42:0.07	1.10:0.41:0.42:0.07
LNTW-15	15	1.15:0.38:0.38:0.10	1.15:0.36:0.38:0.10
LNTW-20	20	1.20:0.33:0.33:0.13	1.20:0.32:0.35:0.14

For the hypothetical binary mixture of "$xLi_{1.6}W_{0.4}O_2$ $(1-x)LiNi_{0.5}Ti_{0.5}O_2$" ($LiMO_2$ formula unit based notation), single phase compositions were achieved for $0 \le x \le 1/3$, adopting the α $LiFeO_2$ type crystal structure, which is schematically shown in Figure 1a. The measured XRD patterns and the refined lattice parameters for a single phase fit in the *Fm*3*m* space group are presented in Figure 1b and Table S1, respectively. Rietveld plots for the X ray refinements of LNT 0 and LNTW X (X = 5, 10, 15, 20) are shown in Figure S1a−e of the Supporting Information (SI). Figure S2 shows transmission electron microscopy (TEM) images for LNT 0 and LNTW 20, revealing small crystallites of size less than 100 nm. Figure 1c shows results from scanning transmission electron microscopy energy dispersive X ray spectroscopy (STEM EDX) mapping for LNTW 20, indicating homoge

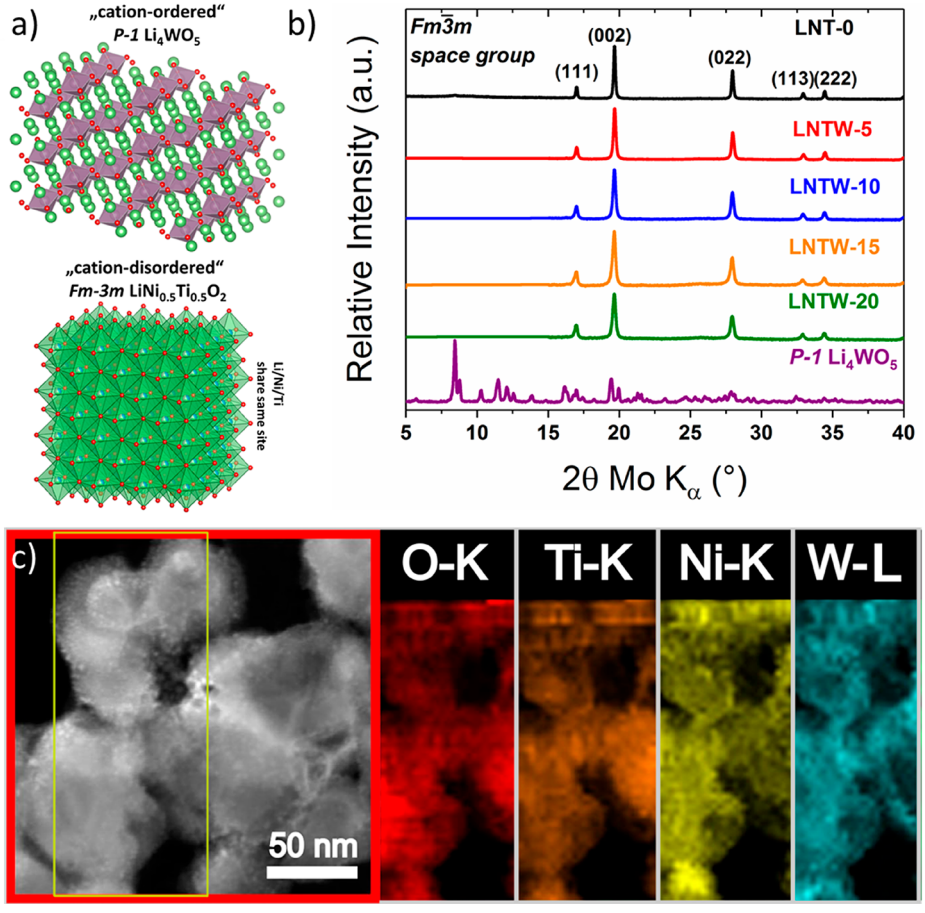

Figure 1. (a) Schematic illustration of crystal structures of rock salt Li_4WO_5 and $LiNi_{0.5}Ti_{0.5}O_2$. (b) XRD patterns of $Li_{1+x/100}Ni_{1/2-x/120}Ti_{1/2-x/120}W_{x/150}O_2$ (x = 0, 5, 10, 15, 20) and Li_4WO_5. (c) STEM EDX elemental mapping of LNTW 20. Note that the crystal structures were drawn using the software VESTA.[44]

neous distribution of Ni, Ti, and W. Note that in disordered rock salts with multiple transition metal species, phase separation may be observed.[43]

Electrochemical Properties. Galvanostatic charge−discharge measurements were carried out to study the electrochemical properties. Figure 2a shows the voltage profiles with the corresponding differential capacity curves for LNT 0, LNTW 5, LNTW 10, LNTW 15, and LNTW 20. The cells were cycled between 4.5 and 1.3 V with a constant specific current of 20 mA g^{-1}. In general, two significant observations were made regarding the shape of the voltage profile and the observed specific capacity. With a gradual increase in Li excess and consequently in the W^{6+} fraction, the shape of the discharge curves altered significantly. For the first charge, a staircase like profile with a distinct voltage plateau around 4.3 V was observed for all compounds. Notably, the voltage plateau became longer with increasing Li excess, resulting in a considerable increase in specific charge capacity. For X > 10, the upper voltage plateau became more sloping, and a more defined lower voltage plateau appeared. For LNTW 15, the lower voltage plateau is located at 1.8 V, whereas LNTW 20 exhibited a more sloping plateau at 2.4 V. LNT 0 delivered a specific discharge capacity of 100 mAh g^{-1} and LNTW X (X = 5, 10, 15, 20) 136, 168, 187, and 226 mAh g^{-1}, respectively. Overall, the discharge capacity increased with Li excess. This observation is in line with percolation theory, which predicts that for disordered rock salts, a Li excess of ≥9% is necessary to form percolating Li sites spanning the entire structure and therefore enables higher lithiation/delithiation degrees.[19,45] The substitution with W^{6+} lowers the fraction of Ni per formula unit, which results in a decrease of the theoretical $Ni^{4+/2+}$ redox, as shown in Figure S3. Notably, in the first charge cycle, LNTW 20 delivered a specific capacity of 246 mAh g^{-1}, clearly exceeding the theoretical Ni^{2+}/Ni^{4+} capacity (Ti^{4+} and W^{6+} have d^0 electron configuration). This implies that other redox species must be involved in the charge compensation mechanism, even though electrolyte/electrode side reactions can also be anticipated for this voltage window. The appearance of the low voltage plateau and the increase in voltage hysteresis have been attributed to structural changes taking place during oxygen oxidation and/or loss.[46]

The cycling stability at 50 mA g^{-1} in the voltage range between 4.5 and 1.3 V is shown in Figure 2b. Striking is that the stability decreased with increasing Li excess. For instance, the LNT 0 cells retained 80% of their initial capacity and delivered a specific discharge capacity of 88 mAh g^{-1} after 50 cycles, whereas LNTW 20 retained only 49% (100 mAh g^{-1}).

In the present work, LNTW 20 was investigated more thoroughly, as it showed the highest capacity among the series of Li−Ni−Ti−W oxides. Figure 2c illustrates the rate performance of LNTW 20. For 50, 100, 200, 400, 800, and 50 mA g^{-1}, LNTW 20 exhibited specific capacities of 205, 153, 111, 60, 35, and 155 mAh g^{-1}, respectively. Figure 2d displays the first cycle charge−discharge profile of each current step.

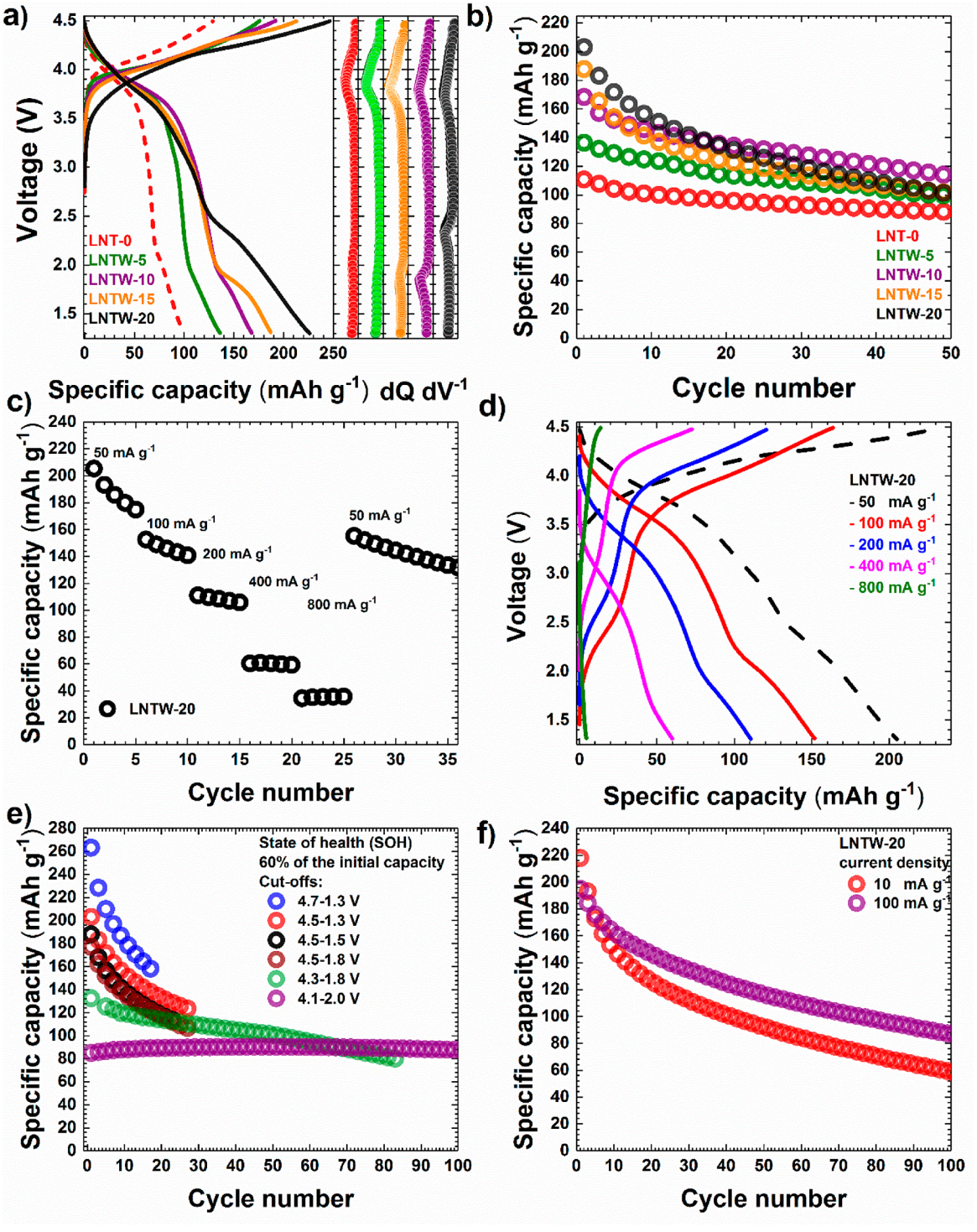

Figure 2. (a) Charge−discharge profiles of LNT 0 and LNTW X (X = 5, 10, 15, 20) with the corresponding differential capacity curves of the discharge cycle at 20 mA g^{-1}. (b) Cycling stability of all compounds when cycled between 4.5 and 1.3 V at 50 mA g^{-1}. (c) Rate capability of LNTW 20 in the range of 4.5−1.3 V and (d) the corresponding charge−discharge profiles of the first cycle for each C rate step. (e) Cycling stability of LNTW 20 for various cutoff voltages at 50 mA g^{-1}. (f) Cycling stability of LNTW 20 cycled between 4.5 and 1.3 V at 10 and 100 mA g^{-1}.

For higher specific currents, we observed a strong increase in polarization and a decrease in specific capacity, thus indicating kinetic limitations.

Furthermore, the cycling stability was examined as a function of the cutoff voltages, which were varied between 4.7 and 1.3 V. Figure 2e shows the cycle life test at 50 mA g^{-1} up to 60% of the initial capacity. For a narrow voltage window of 4.1−2.0 V, a reasonably stable cycling behavior was observed, however, with a relatively low specific discharge capacity of 85 mAh g^{-1}. In contrast, the extended voltage window of 4.7−1.3 V led to a relatively high specific discharge capacity of 263 mAh g^{-1}, but at the cost of accelerated fading (note that the capacity dropped to 60% within 17 cycles). Figure 2f shows the cycling stability of LNTW 20 for specific

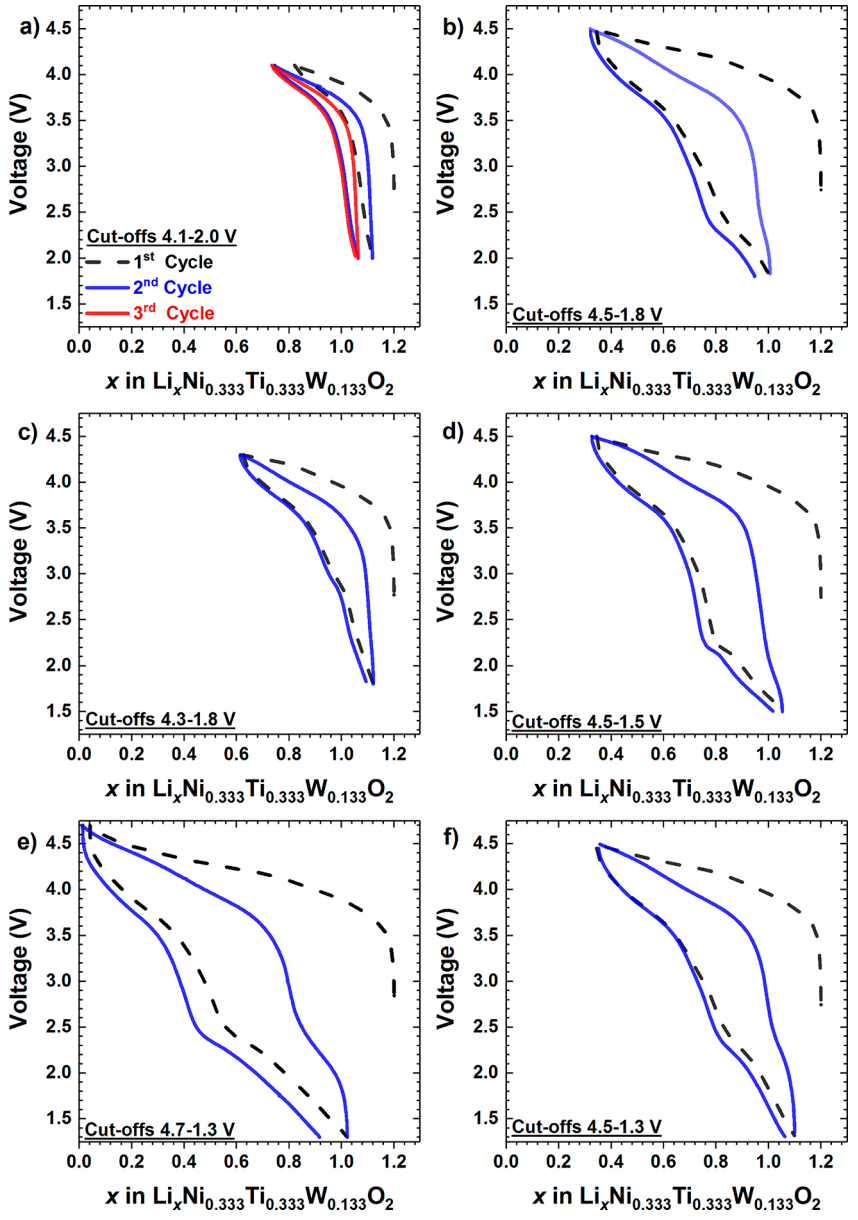

Figure 3. Charge−discharge profiles of LNTW 20 at 50 mA g^{-1} for various cutoff voltages: (a) 4.1−2.0 V, (b) 4.5−1.8 V, (c) 4.3−1.8 V, (d) 4.5−1.5 V, (e) 4.7−1.3 V, and (f) 4.5−1.3 V.

currents of 10 and 100 mA g^{-1} in the voltage range between 4.5 and 1.3 V. The cells delivered 59 mAh g^{-1} and retained 27% of the maximum capacity after 100 cycles at 10 mA g^{-1}. After the same number of cycles, the cells could deliver 87 mAh g^{-1} at 100 mA g^{-1}, corresponding to 45% of the initial capacity. It is noteworthy that the capacity retention is lower for slower cycling and increases with the current density. This could hint at reactive interactions between the electrode and electrolyte. Slower rates infer longer contact times with the electrolyte and therefore less reaction and more time for self discharge via oxygen release.[26,28,47,48]

Figure 3 shows the respective charge−discharge profiles for various cutoff voltages. In Figure 3a, c, and e, the lower and upper cutoff voltages were gradually decreased and increased, respectively, with each scan starting from the open circuit voltage of 2.8 V. When the voltage range was limited between 4.1 and 2.0 V, the profiles remained relatively symmetric with low voltage hysteresis. A noticeable and increasing hysteresis was observed when the voltage window was increased. When the upper cutoff was set to 4.5 V and the lower cutoff was decreased (deeper discharge), the hysteresis remained fairly large, as shown in Figure 3b, d, and f (see also changes in voltages profiles with prolonged cycling in Figure S4). This observation points to a voltage hysteresis triggered with charging beyond 4.1 V. Similar observations have been made for other lithium rich materials, and both oxygen redox and lattice oxygen loss, leading to surface reconstruction, have been inferred as the underlying reasons.[49]

In order to determine whether oxygen release took place in the case of LNTW 20, *in situ* DEMS measurements were performed and the results compared to LNT 0. To this end, half cells were charged at a specific current of 10 mA g^{-1} for LNT 0 and 16 mA g^{-1} for LNTW 20 while monitoring the gas evolution. Figure 4 shows the voltage and gas evolution profiles for the first three cycles. For LNTW 20, CO_2 evolution started around 3.9 V in the initial (activation) cycle, and as expected,

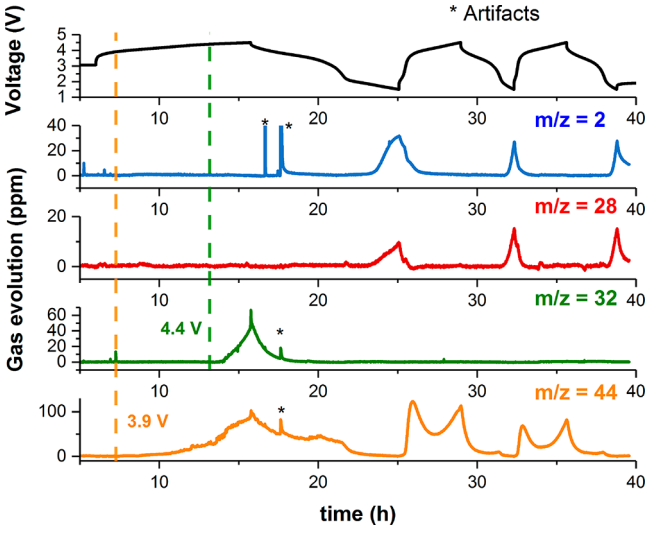

Figure 4. DEMS measurement for the first three cycles of an LNTW 20 half cell. The cell voltage (black) is shown together with the m/z = 2 (H_2 in blue), m/z = 28 (C_2H_4 in red), m/z = 32 (O_2 in green), and m/z = 44 (CO_2 in orange) evolution. Artifacts are denoted by asterisks.

the evolution rate decreased in the later cycles. Interestingly, the DEMS data reveal two maxima in the second and third cycles, which appear to be associated with the low and high voltage plateaus during charge. Significant O_2 evolution was only observed above 4.4 V in the first charge cycle, thereby indicating oxygen loss from the lattice. Upon discharge (initial cycle), the formation of C_2H_4 and H_2, due to reductive decomposition of the electrolyte, was clearly observed below 2.0 V, with the highest evolution rates at the lower cutoff voltage.[50] The comparison with LNT 0 in Figure S5 demonstrates that apparent oxygen evolution only occurs for the lithium excess material. Note that side reactions of released oxygen with the electrolyte are not the only source of CO_2, as similar behavior was observed for both compounds. Electrochemical electrolyte oxidation[51] and decomposition of carbonate contaminates[52,53] from the synthesis can also contribute to CO_2 evolution. In Li rich compounds, oxygen loss has been shown to occur predominantly at the surface of the active material particles, eventually leading to the formation of densified surface phases.[54−56]

Structural Changes upon Cycling. *In situ* XRD measurements were carried out to investigate the structural changes of LNTW 20 and LNT 0 in the first charge−discharge and second charge cycles between 4.5 and 1.5 V at 16 and 10 mA g^{-1}, respectively. The voltage profile and the changes in the *a* lattice parameter from single phase Rietveld refinement analysis are shown in Figure 5 and Figure S6 with an enlarged section of the 002 reflections. During the initial charge of LNTW 20, two distinct regimes were found. The first one starts from the open circuit voltage of 2.8 V and extends to 4.0 V and shows a strong slope, where the *a* lattice parameter decreases continuously (thus reflecting lattice contraction).

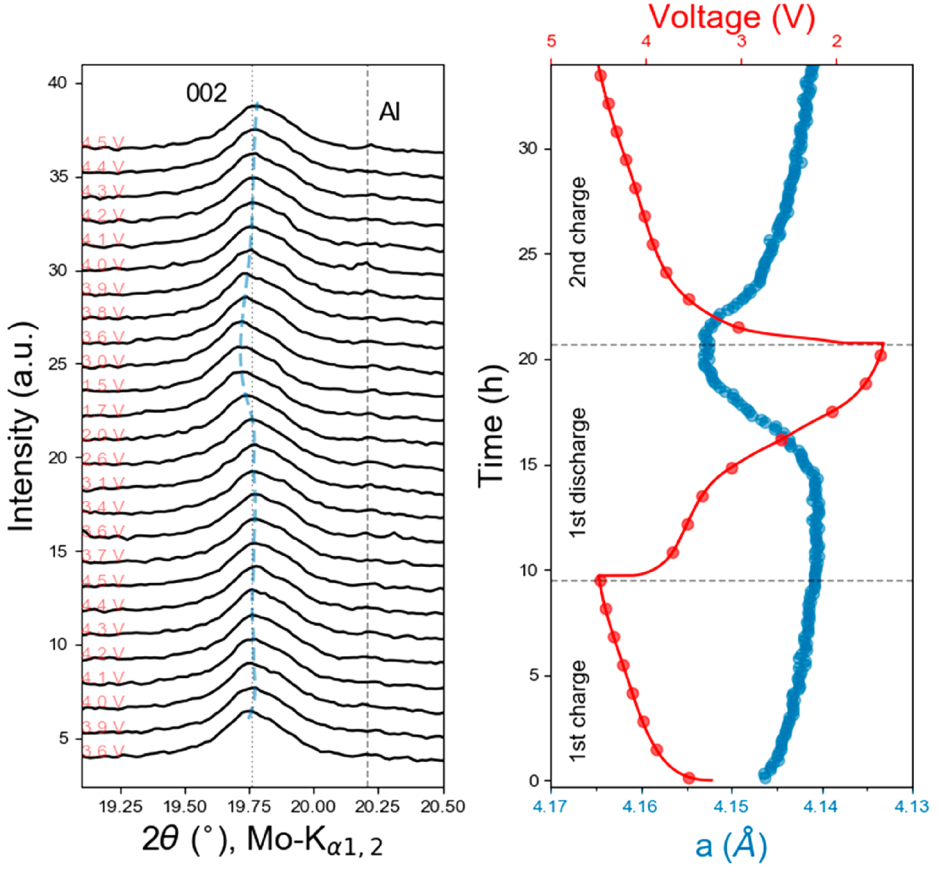

Figure 5. *In situ* XRD patterns of LNTW 20 over two consecutive cycles in the voltage range of 4.5−1.5 V with the corresponding voltage profile (red) and changes in the *a* lattice parameter (blue) from Rietveld refinement analysis. The red dots represent the measurement points where the XRD patterns were collected.

Table 2. Parameters of the Single Shell EXAFS Fits

state	shells	$N S_0^2$	σ^2 (10^{-4} Å^2)	R_{W-O} (Å)	ΔE_0 (eV)
pristine	W O	2.5 ± 0.1	43 ± 5	1.79 ± 0.01	4.3 ± 1.8
discharged	W O	2.12 ± 0.08	18 ± 3	1.76 ± 0.01	2.8 ± 1.4
charged	W O	1.8 ± 0.2	17 ± 9	1.74 ± 0.02	3.5 ± 3.8
charged[a]	W O_1	1.8 ± 0.2	20[b]	1.73 ± 0.01	0[b]
	W O_2	0.8 ± 0.3		2.15 ± 0.03	

[a]Results for the fit assuming two W−O shells. [b]Fixed value.

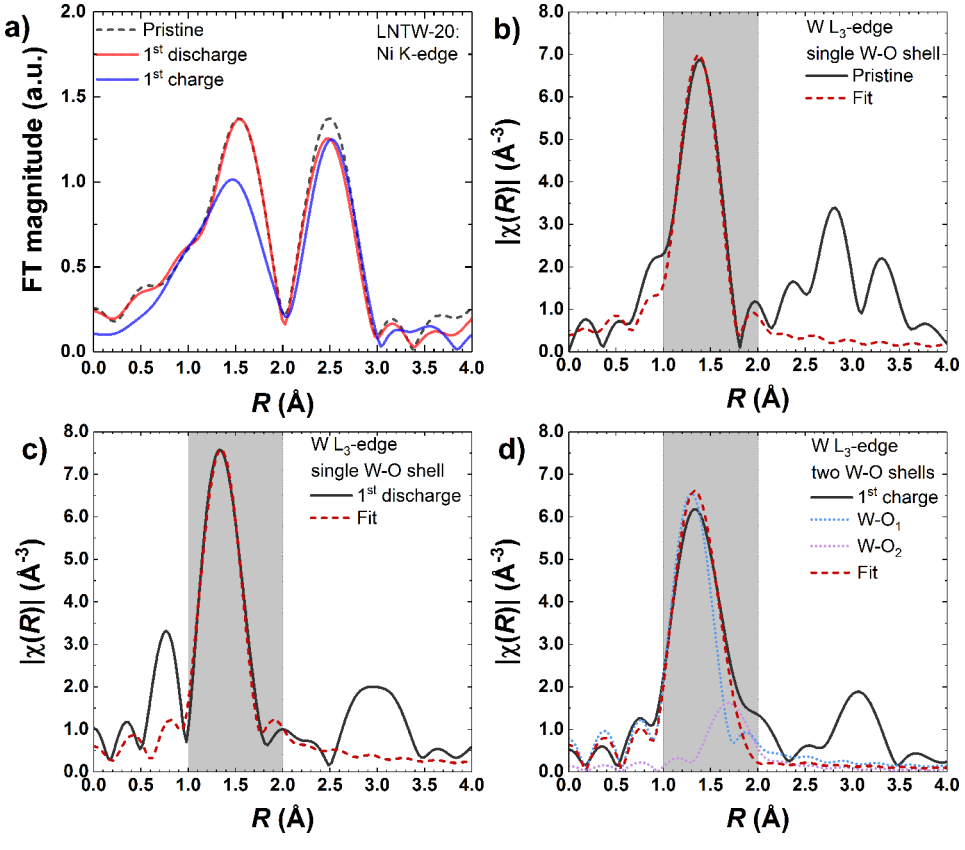

Figure 6. FT EXAFS of LNTW 20. (a) Ni K edge for the pristine, fully charged, and fully discharged states. W L_3 edge with the corresponding fit for the (b) pristine, (c) discharged, and (d) charged states.

This finding can be related to $Ni^{2+/3+}$ oxidation [Ni^{2+} (r = 0.69 Å) and Ni^{3+} (r = 0.56 Å)].[57] Beyond 4.0 V, the lattice parameter changes only slightly until the end of charge. Oxygen oxidation and release can be anticipated, as shown by DEMS. O^{2-} oxidation may result in shrinkage of the oxygen framework due to shortened interatomic distances as a consequence of the elimination of electrons from antibonding states of the σ^* orbital.[58] During the first discharge from 4.5 to 3.1 V, the a lattice parameter remains nearly constant. From 3.1 to 1.7 V, it changes significantly due to lattice expansion, and from 1.7 to 1.5 V, the changes are minor. At the end of the first discharge, the a lattice parameter was found to be slightly larger as compared to the pristine material. At the beginning of the second charge cycle, a rapid decrease from 4.153 to 4.149 Å at 3.5 V was observed. During further charging, the evolution of the a lattice parameter closely resembles the behavior of the initial cycle. For LNT 0, the a lattice parameter shows slight changes with a monotonous decrease during charge and monotonous increase during discharge (see Figure S6). In contrast to LNTW 20, there is no direct evidence of oxygen loss for LNT 0 by DEMS, which provides a likely explanation for the differences in the evolution of the a lattice parameters.

For further clarification of the structural changes, the local structure of Ni and W was probed by EXAFS. The EXAFS fitting procedure for the first coordination shell is described in the SI, and the fitting parameters are given in Table 2. Figure 6a displays the Fourier transform (FT) of the Ni K edge. The maximum at 1.5 Å corresponds to the first oxygen coordination shell (Ni−O) and the second maximum at 2.5 Å to the sphere with Ni atoms (Ni−Ni). During charge, the most pronounced changes take place in the first coordination shell around the Ni atoms, resulting in a decrease of the Ni−O peak amplitude. This can be explained by the distortion of the oxygen octahedron around Ni^{3+} due to Jahn−Teller distortion, where two bonds are elongated, thus reducing the effective coordination number upon oxidation.[59,60] When Ni^{3+} is reduced back to Ni^{2+}, the Ni−O peak amplitude is increased again. For LNTW 20, the Ni−O peak amplitude recovers fully, indicating the reversibility of the reaction.

Figure 6b−d and Figure S7a display the FT of the W L_3 edge (k^3 weighted EXAFS in R space) with first shell fits for

LNTW 20 at different states of charge (SOC). Table 2 reports the parameters refined during the fitting and includes the coordination number, correlated with the amplitude reduction factor S_0^2,[61,62] energy shift parameter ΔE_0, bond length $R_{(W-O)}$, and Debye–Waller factor σ^2. The changes in the first coordination number were estimated using the product $N \cdot S_0^2$, as these two parameters are correlated. Furthermore, to avoid correlation between coordination number and Debye–Waller factor (represents the thermal and static disorder in the bond distances), we applied the strategy shown in Figure S7b–d when σ^2 is calculated for different $N \cdot S_0^2$ using three k weights. The correlation between these parameters can be eliminated, given that σ^2 exhibits a k weight dependence unlike $N \cdot S_0^2$. Proper values for $N \cdot S_0^2$ and σ^2 were therefore chosen in the points of intersection. The fits for the pristine and discharged samples shown in Figure 6b and c were made using a single W–O shell. For the charged state, such a fit provided poor agreement with the experimental data (cf. Figure S7a). An additional lowering of $N \cdot S_0^2$ suggests a splitting of the oxygen shell. Clearly, the two W–O shell model with independent distances and amplitudes captures the data more accurately, as shown in Figure 6d. The number of independent points N_{idp} was preserved by fixing ΔE_0 to 0 and σ^2 to 0.002 Å^2 for both scattering paths, resulting in two oxygen shells with $N \cdot S_0^2$ amplitudes of 1.8 ± 0.2 and 0.8 ± 0.3 at distances (R_{W-O}) 1.73 ± 0.01 Å and 2.15 ± 0.03 Å, respectively. Compared to the single shell fit with the same number of independent variables, the R factor decreased from 0.052 to 0.012, and χ^2 decreased from 286 to 64, indicating better suitability of the model. Upon charge, a rearrangement in the first coordination shell of W–O takes place with two distinctly different but close W–O oxygen bonds, leading to an apparent reduction in $N \cdot S_0^2$ for the single W–O shell model ("charged" in Table 2). However, the two shell model ("charged[a]" in Table 2) clearly demonstrates that the oxygen coordination number in the charged sample is similar to the pristine one. In contrast to the discharged sample, a significant reduction in $N \cdot S_0^2$ was observed compared to the pristine sample. We attribute this result to the formation of oxygen vacancies around W.

Redox Mechanism. In order to elucidate the redox mechanism, a combination of DFT calculations with *ex situ* XAS and XPS was used. For LNTW 20, only Ni is expected to be redox active since Ti^{4+} and W^{6+} are d^0 elements that cannot contribute to the charge compensation in the lithiated (discharged) state. Interestingly, LNTW 20 delivered 246 mAh g^{-1} in the first charge (delithiation) cycle, corresponding to 0.92 Li per formula unit (f.u.), thus exceeding the theoretical capacity of $Ni^{2+/4+}$ redox (178 mAh g^{-1}). This implies that other species are involved in the charge compensation mechanism (Ti^{4+} and W^{6+} are electrochemically inactive during the first charge).[27]

Figure 7 compares the equilibrium voltage profile predicted by DFT with the experimental measurement. The calculated voltage traces the measured first charge voltage well but slightly underestimates it by ~0.4 V. The computed voltage profile shows a continuous slope until 166 mAh g^{-1} and a voltage plateau for higher capacities. This indicates that the redox mechanism changes from a single phase to a two phase reaction after 0.667 out of 1.2 Li per f.u. have been extracted. Further analysis of the magnetic moment of the nickel and oxygen atoms during delithiation (Figure S8) revealed that the sloped region of the voltage profile corresponds to Ni redox,

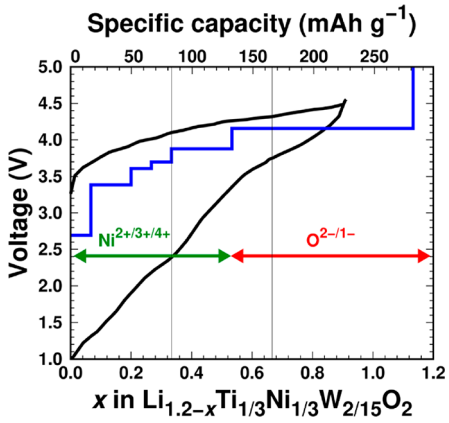

Figure 7. Calculated voltage profile (in blue) of LNTW 20 as predicted by DFT. The measured voltage profile is overlaid (black lines). Vertical lines indicate the theoretical capacity for $Ni^{2+/3+}$ and $Ni^{3+/4+}$ redox. The redox regions predicted by DFT, i.e., nickel or oxygen oxidation, are indicated by green and red arrows. Further details of the DFT calculations are given in the Experimental Section.

whereas the voltage plateau is mostly due to oxygen oxidation. The calculations predict that nickel is not fully oxidized to Ni^{4+}. This finding is in agreement with previous computations that cation disorder can raise the $Ni^{3+/4+}$ redox potential.[63] Only around 60% of the theoretical $Ni^{3+/4+}$ redox capacity is accessed before oxygen oxidation dominates. Note that the calculated voltage profile predicts a higher overall accessible capacity than is observed in the experiment since the computations did not account for oxygen loss and subsequent structural changes.

The Ni K edge X ray absorption near edge structure (XANES) data for different SOCs shown in Figure 8a and Figure S9 confirm that the edge position is similar to charged $LiNi_{0.5}Ti_{0.5}O_2$ with roughly 0.5 Li per f.u. extracted (based on the charge capacity) and therefore close to a Ni^{3+} oxidation state. Note that the ratio of Ni^{3+} to Ni^{4+} cannot be determined quantitatively. During discharge, the Ni K edge shifts back to lower energies, pointing to nickel reduction. Interestingly, it was observed that oxygen loss occurred together with the partial reduction of Ni^{3+} to Ni^{2+}.[35] This could explain the relatively smaller shifts of the Ni K edge generally found for Ni based disordered rock salts. Figure 8b shows the L_3 edge of W for different SOCs and the model compounds WO_2 and WO_3. The W L_3 edge white line exhibits prominent 2p s and 2p d dipole allowed electronic transitions, originating primarily from $2p_{3/2}$ to $5d_{5/2}$ states with a weaker contribution of $2p_{3/2}$ to $5d_{3/2}$.[64] For the W L_3 edge, the most striking difference is a change in the amplitude and broadening of the white line. The amplitude may reflect structural distortion and therefore splitting of the d states manifold, which changes the number of unoccupied 5d states. The shape of the white line could suggest deviation from the octahedral symmetry of the W local environment since it is not distinctly split.[65,66] However, W L_3 XANES alone is not sufficient to determine the oxidation state.[64] Hence, XPS was used to probe the surface oxidation state of tungsten and titanium for LNTW 20 in the pristine and charged states, and the results obtained are shown in Figure 8c, d, e, and f. For the pristine compound, single peak doublets at 458.3/464.0 eV for Ti 2p and 35.8/38.0 eV for W 4f were introduced for the peak fits in these regions, i.e., both Ti and W were in the expected oxidation state of +4 and +6,

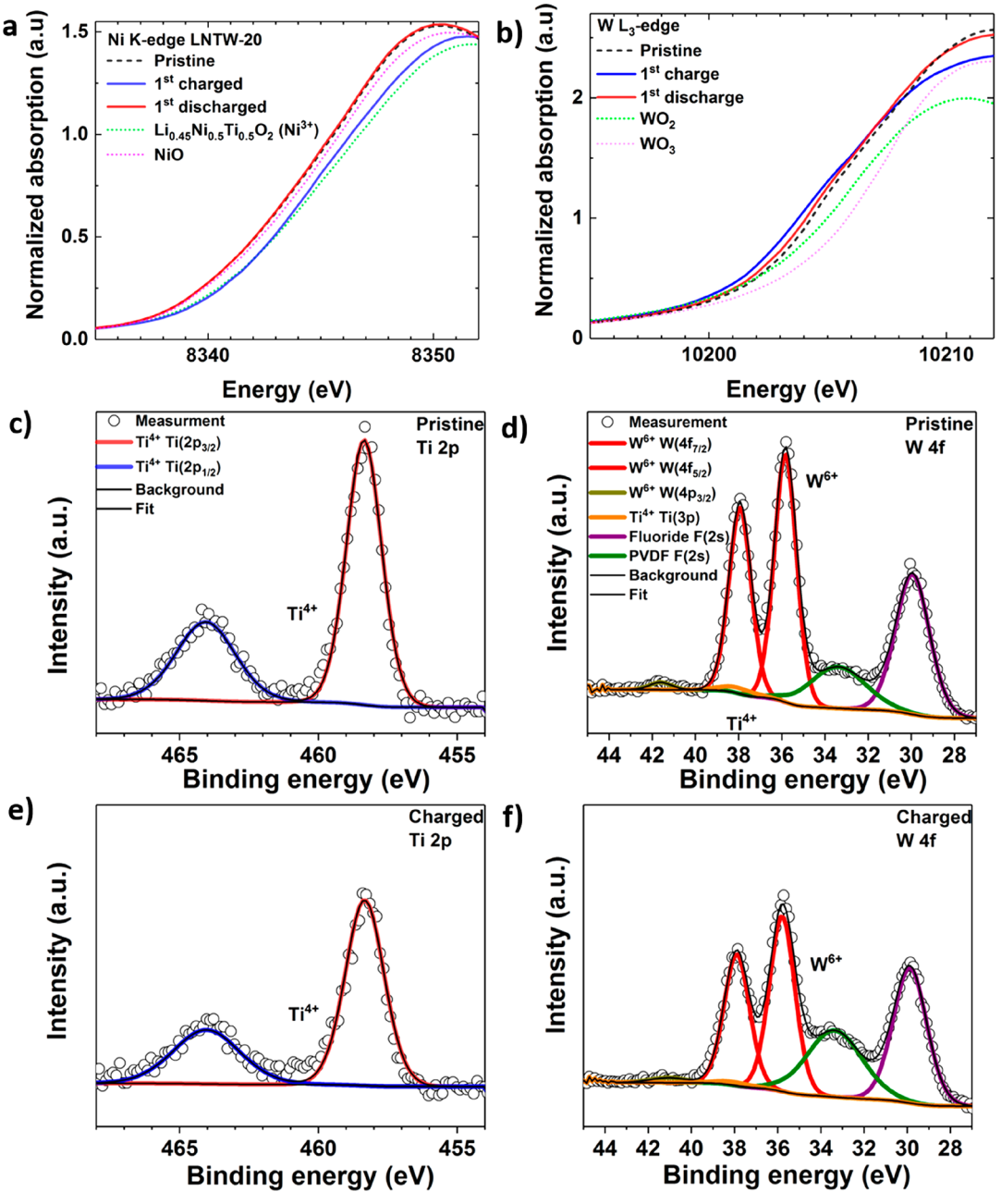

Figure 8. Experimental XANES and XPS spectra for LNTW 20 at different SOC. (a) Ni K edge, (b) W L_3 edge, (c and e) Ti 2p core level spectra, and (d and f) W 4f core level spectra. The intensity of the Ti 3p peak was determined by comparison with the Ti 2p peak taking the relative sensitivity factors of both peaks into account.

respectively. The F 1s spectrum from the pristine electrode in Figure S10 displays two peaks at ~688 and 685 eV, which can be assigned to fluorine in PVDF and LiF, respectively.[67] We were not able to detect a change of the oxidation state of Ti and W in the charged sample. However, note that the F 2s peaks of PVDF and LiF obscure the energy range at which the W $4f_{7/2}$ peak component of W in lower oxidation state would be expected to appear (e.g., ~32.8 eV for W^{4+}). If an additional W 4f peak doublet accounting for W^{4+} is added to the fit (fixed at 32.8 and 35.0 eV), its intensity amounts to less than 10% of that of the W^{6+} doublet. This means the presence of a small number of W atoms in the reduced state cannot be excluded on the basis of this measurement. Interestingly, partial reduction of the Mo^{6+} to Mo^{4+} has been found for the Mo analog system $Li_{1.2}Ni_{0.333}Ti_{0.333}Mo_{0.133}O_2$ and associated with oxygen loss on the surface.[24]

Oxygen Activity and Voltage Hysteresis in Ni-Based Compounds. Ni based disordered rock salts showing both anionic and cationic redox such as $Li_{1.2}Ni_{0.333}Ti_{0.333}Mo_{0.133}O_2$,[33] $Li_{1.3}Ni_{0.27}Nb_{0.27}O_2$,[20] $Li_{1.2}Ti_{0.35}Ni_{0.35}Nb_{0.1}O_{1.8}F_{0.2}$,[40] and $Li_{1.3}Ni_{0.27}Ta_{0.43}O_2$[35] suffer from severe capacity fading. All these compounds have in common that they have Li excess introduced with a high valence d^0 cation and show oxygen redox and/or oxygen loss, with limited utilization of the $Ni^{4+/2+}$ redox couple and large voltage hysteresis between charge and discharge. On the contrary, $Mn^{4+/2+}$ redox was realized in disordered rock salt compounds containing d^0 cations with comparably low voltage

hysteresis. Several different hypotheses regarding the origin of the voltage hysteresis, in particular, the appearance of the low voltage plateaus during discharge, have been suggested in the literature.[35,68−72] However, only a few studies were performed for disordered rock salt systems. In general, the voltage hysteresis has been attributed to structural modifications related to cation migration or anionic redox. Lee et al.[33] ascribed the appearance of a low voltage plateau in $Li_{1.2}Ni_{0.333}Ti_{0.333}Mo_{0.133}O_2$ to a kinetic inhibition due to surface densification after the loss of oxygen. They hypothesized that the associated loss of Li excess results in kinetic limitations, thus leading to a high voltage polarization, based on an estimate of the redox contribution of Mo^{y+} and Ti^{x+} in the surface regions from the amount of O loss. In contrast, Jacquet et al.[35] attributed the instability of Ni based compounds against O_2 release and the large hysteresis (due to the low voltage plateau associated with oxygen reduction) to the low charge transfer bandgap associated with the Jahn−Teller distorted Ni^{3+}. A small charge transfer bandgap, in conjunction with anion oxidation, may facilitate electron transfer from σ^* states of O to the transition metal, leading to a reduction of the transition metal and O_2 release.[71,73] Supporting this hypothesis, Taylor et al.[74] associated the voltage drop and the low voltage plateau observed for $Li_{4.15}Ni_{0.85}WO_6$ with the formation of peroxide like oxygen dimers (d_{O-O} = 1.46 Å); the role of d^0 W^{6+} in the stabilization of peroxide species in Li rich rock salts was highlighted.

Nevertheless, the question of what triggers oxygen loss remains interesting. Bruce et al.[75,76] proposed that oxygen loss occurs when the average coordination number around the oxygen anion falls below 3 (i.e., a high degree of alkali deficiency during charge), which has been exemplified for P2−$Na_{0.78}Li_{0.25}Mn_{0.75}O_2$ (oxygen release) and P2−$Na_{0.67}Mg_{0.28}Mn_{0.72}O_2$ (no oxygen loss), both showing oxygen redox. Interestingly, although no oxygen loss occurs for P2−$Na_{0.67}Mg_{0.28}Mn_{0.72}O_2$, a large voltage hysteresis is observed. However, the hysteresis has been correlated not only with oxygen redox and/or oxygen loss but also with cation migration.[77] Gent et al.[78] proposed a mechanism, where transition metal migration is the consequence of oxygen redox, thereby linking oxygen redox with cation migration. Striking is the finding that the voltage hysteresis related to oxygen redox can be small for structures inhibiting the local transition metal disorder, thus preventing oxygen dimerization and O_2 formation.[79−81] These findings underline the impact of local cation environment on the cationic and anionic redox potentials. Different approaches, such as the incorporation of fluorine[46] in the anion lattice and surface modification,[24] have been tested with moderate success in the mitigation of oxygen loss and voltage hysteresis. In this context, it is important to note that identifying the underlying reasons for the complex processes, which vary with the cations and are clearly dependent on the local environment, is very challenging and clearly requires more studies.

CONCLUSIONS

In summary, rational design principles for the solid solution series $Li_{1+x/100}Ni_{1/2-x/120}Ti_{1/2-x/120}W_{x/150}O_2$ (x = 0, 5, 10, 15, 20) have been introduced as a new class of high capacity disordered rock salt oxides. In agreement with a recent percolation theory model, we observe that the specific capacity increases with the amount of lithium excess. $Li_{1.2}Ni_{0.333}Ti_{0.333}W_{0.133}O_2$ delivers up to 225 mAh g^{-1} and 675 Wh kg^{-1} at 20 mA g^{-1} in the initial cycle. On the basis of combined characterization data from *in situ* XRD, XANES, EXAFS, DEMS, XPS, and electrochemical cycling, we propose that the redox mechanism is a combination of $Ni^{2+/3+}$ and possibly a partial Ni^{4+} reservoir for charge compensation. According to DFT calculations, Ni redox accounts theoretically for 119 mAh g^{-1} but is not sufficient to explain the measured specific capacity of 246 mAh g^{-1} during the first charge. Oxygen loss is evident from the oxygen evolution detected by DEMS. Although the release of lattice oxygen can be regarded intuitively as the irreversible part of anion redox, the exact relationship between oxygen loss and oxygen redox has not yet been clarified. After oxygen loss, W^{6+} and Ti^{4+} can possibly participate in the charge compensation, which has been evidenced for an analog Mo based material system.[24,33] We argue that the capacity fading mechanism is closely linked to the oxygen loss and the associated structural changes. In addition, oxygen loss results in higher surface reactivity toward the electrolyte. Similar observations have been made for other Ni based disordered rock salts, suffering from oxygen loss and large hysteresis and thus pointing to electronic instabilities related to the presence of Jahn−Teller active Ni^{3+}.

EXPERIMENTAL SECTION

Synthesis. For the synthesis of $Li_{1+x/100}Ni_{1/2-x/120}Ti_{1/2-x/120}W_{x/150}O_2$ (x = 0, 5, 10, 15, 20), Li_2CO_3 (Alfa Aesar, 99%), $NiCO_3$ (Alfa Aesar, 99%), TiO_2 nanopowder (<50 nm; Alfa Aesar, 99.7%), and WO_3 (Alfa Aesar, 99%) were used as precursors. Li_4WO_5 was synthesized using adapted conditions. The precursors were ball milled for 24 h at 200 rpm using a Fritsch P6 planetary ball mill with a 80 mL silicon nitride vial and silicon nitride balls, with a ball to powder weight ratio of 20:1. Subsequently, the milled mixture was pelletized and then sintered at 900 °C for 2 h in air, followed by furnace cooling to 200 °C and immediate transfer inside an argon filled glovebox. Li_4WO_5 was sintered at 650 °C for 24 h. After sintering, the pellets were manually ground into a fine powder.

Density Functional Theory (DFT). DFT calculations were performed using the Vienna Ab Initio Simulation Package (VASP).[82,83] All calculations employed a plane wave basis set with an energy cutoff of 520 eV for the representation of the Kohn−Sham orbitals, Gamma centered k point meshes with a spacing of 25 $Å^{-1}$ for the Brillouin zone integration, and projector augmented wave pseudopotentials.[84] A structure model of composition $Li_{18}Ni_5Ti_5W_2O_{30}$ ($Li_{1.2}Ni_{1/3}Ti_{1/3}W_{2/15}O_2$) was used to model the fully lithiated LNTW 20, and possible atomic orderings were enumerated using the method by Hart and co workers,[85,86] as made available by the Python Materials Genomics (pymatgen) package.[87] Out of around 30 000 enumerated configurations, 350 configurations were randomly selected for DFT calculations to identify a representative low energy atomic ordering that was used as the initial structure for subsequent delithiation, considering a total of 650 delithiated structures with enumerated lithium vacancy orderings.

The 1000 DFT calculations of enumerated structure models employed the exchange correlation functional by Perdew, Burke, and Ernzerhof (PBE)[88] with an additional rotationally invariant Hubbard U correction[89,90] for the nickel d bands. The U value of 6.0 eV by Jain et al.[91] was used. While PBE+U is accurate for predicting transition metal redox reactions, it is not reliable for oxygen redox. Structures predicted to be low in energy by PBE+U were therefore recalculated using the Strongly Constrained and Appropriately Normed (SCAN) exchange correlation functional,[92] which has been shown to predict accurate formation energies of transition metal oxides even without Hubbard U correction.[93] All reported computational results are based on SCAN calculations.

The equilibrium voltage of the delithiation reaction $Li_{x_1}MO_2 \rightarrow Li_{x_2}MO_2 + (x_1 - x_2)Li^+ + (x_1 - x_2)e^-$ was calculated using Nernst's equation but neglecting temperature effects[94,95]

$$\bar{V} \approx -\frac{E(Li_{x_1}MO_2) - E(Li_{x_2}MO_2) - (x_1 - x_2)E(Li)}{(x_1 - x_2)F}$$

where $E(Li_xMO_2)$ is the DFT energy of LNTW 20 with lithium content x, $E(Li)$ is the DFT energy of lithium metal in the body centered cubic crystal structure, and F is the Faraday constant. Only the compositions predicted to be thermodynamically stable, as determined by a convex hull construction of the formation energy (Figure S11), occur in the voltage profile.

Electrochemical Testing. Electrochemical tests were carried out in Swagelok type cells. Electrode slurries were made of 90 wt % composite and 10 wt % polyvinylidene difluoride (PVDF) binder with *N* methyl 2 pyrrolidone (NMP) as a solvent. The composites comprised active material and Super C65 carbon black in a weight ratio of 80:20. The mixed slurry was coated onto an aluminum foil using the doctor blade technique and dried at 120 °C for 12 h in a vacuum. Each working electrode (12 mm diameter) contained approximately 3 mg of active material, and Li foil was used as a counter electrode. LP30 from BASF SE (ethylene carbonate/dimethyl carbonate, 1:1 weight ratio with 1 M $LiPF_6$) was used as an electrolyte. Temperature controlled galvanostatic charge−discharge experiments were conducted at 25 °C in climate chambers using an Arbin electrochemical workstation.

Differential Electrochemical Mass Spectrometry (DEMS). *In situ* gas analysis was performed by use of DEMS. The setup has been described elsewhere.[51,96] Custom made cells with gas in and outlets were assembled in an argon filled glovebox. The (circular) cathodes used had a diameter of 40 mm with a 4 mm hole for proper gas extraction. GF/A (42 mm diameter; GE Healthcare Life Sciences, Whatman) was used as a separator; 600 μL of LP47 (1 M $LiPF_6$ in ethylene carbonate/diethyl carbonate, 3:7 by weight, BASF SE) as an electrolyte; and 40 mm diameter, 600 μm thick Li metal foil (Albemarle Germany GmbH) as a counter electrode. A constant carrier gas flow (2.5 mL_{He} min^{-1}; purity 6.0) was applied during the DEMS measurements for gas extraction. The gas was analyzed by mass spectrometry (GSD 320; OmniStar Gas Analysis System, Pfeiffer Vacuum GmbH). After each run, a calibration gas of known composition was introduced to quantify the measured ion currents.

X-ray Absorption Spectroscopy (XAS). The P65 XAS beamline (PETRA III, Hamburg) provides a relatively large beam (0.5 × 1 mm^2) and a moderate photon flux density. The 11 period mini undulator delivers a monochromatic photon flux of about 10^{11} ph s^{-1}. Two plane mirrors with variable angle of incidence and three different surface coatings are installed in front of the water cooled double crystal monochromator. Si(111) and Si(311) crystals are used for the energy ranges 4−22 keV and 7−44 keV, respectively. The P65 beamline is also equipped with a seven pixel HPGe energy dispersive detector and Si PIPS diode. XAS measurements were performed in both transmission and fluorescence mode. For *ex situ* measurements, the step scan mode with a duration of 10−11 min for each spectrum was utilized.

Extended X-ray Absorption Fine Structure (EXAFS). Single shell Fourier fitting of EXAFS data was performed in the Demeter package[97] using theoretical amplitudes and phases calculated by the FEFF6 code.[98] The fit was done in R space from 1.0 to 2.0 Å using the Fourier transformed k^2 weighted $\chi(k)$ data applying a Δk Hanning window from 2.0 to 11.0 $Å^{-1}$ with a width of the window slope dk = 0.2 $Å^{-1}$. The fitting parameters were the first shell W−O interatomic distance (R_{W-O}), Debye−Waller factor (σ^2), zero energy shift (ΔE_0), and the product of coordination number and amplitude reduction factor $N{\cdot}S_0^2$. To reduce the observed correlations between σ^2 and $N{\cdot}S_0^2$, the σ^2 (N,S_0^2) dependencies for differently k weighted data were plotted, and the chosen values defined by the intersection of the three lines.

X-ray Diffraction (XRD). *In situ* XRD patterns were collected using modified coin cells on a parallel beam laboratory diffractometer with a microfocus rotating anode (Mo Kα radiation) in transmission geometry and a Pilatus 300 K−W area detector. The cells consisted of a LNTW 20 based cathode, Li anode, LP30 electrolyte, and Whatman glass fiber film separator. Galvanostatic charge−discharge cycling was performed in the range between 1.5 and 4.5 V using an Ivium potentiostat. Diffraction patterns were collected every 300 s. Two consecutive patterns were coadded to eliminate cosmic spikes on the detector. The diffraction images were integrated using the pyFAI software[99] and analyzed with the Rietveld method using software TOPAS V6.

X-ray Photoelectron Spectroscopy (XPS). The elemental composition of the surface region was analyzed by XPS using a Physical Electronics PHI 5800 ESCA system. The measurements were carried out with monochromatic Al K_a radiation (250 W, 13 kV) at a detection angle of 45° and with pass energies of 93.9 and 29.35 eV for survey and detailed measurements, respectively. An electron flood gun was used for sample neutralization. The main C 1s peak was set to 284.8 eV for binding energy calibration. Some of the samples were subject to Ar^+ ion sputtering (approximately 1 nm min^{-1} sputter rate, 1 mA, 5 kV) to remove the topmost surface layer(s).

AUTHOR INFORMATION

Corresponding Author

Maximilian Fichtner − *Helmholtz Institute Ulm (HIU) Electrochemical Energy Storage, 89081 Ulm, Germany; Institute of Nanotechnology, Karlsruhe Institute of Technology (KIT), 76344 Eggenstein Leopoldshafen, Germany*;
Email: m.fichtner@kit.edu

Authors

Musa Ali Cambaz − *Helmholtz Institute Ulm (HIU) Electrochemical Energy Storage, 89081 Ulm, Germany*;
orcid.org/0000 0002 4249 3486

Alexander Urban − *Department of Chemical Engineering, Columbia University, New York, New York 10027, United States*

Syed Atif Pervez − *Helmholtz Institute Ulm (HIU) Electrochemical Energy Storage, 89081 Ulm, Germany*;
orcid.org/0000 0002 7134 7103

Holger Geßwein − *Institute for Applied Materials, Karlsruhe Institute of Technology (KIT), 76344 Eggenstein Leopoldshafen, Germany*

Alexander Schiele − *Institute of Nanotechnology, Karlsruhe Institute of Technology (KIT), 76344 Eggenstein Leopoldshafen, Germany*
Alexander A. Guda − *The Smart Materials Research Institute, Southern Federal University, 344090 Rostov on Don, Russia;* orcid.org/0000 0002 6941 4987
Aram L. Bugaev − *The Smart Materials Research Institute, Southern Federal University, 344090 Rostov on Don, Russia; Southern Scientific Centre, Russian Academy of Sciences, 344006 Rostov on Don, Russia;* orcid.org/0000 0001 8273 2560
Andrey Mazilkin − *Institute of Nanotechnology, Karlsruhe Institute of Technology (KIT), 76344 Eggenstein Leopoldshafen, Germany; Institute of Solid State Physics of the Russian Academy of Sciences, 142432 Chernogolovka, Russia*
Thomas Diemant − *Institute of Surface Chemistry and Catalysis, Ulm University, 89081 Ulm, Germany*
R. Jürgen Behm − *Helmholtz Institute Ulm (HIU) Electrochemical Energy Storage, 89081 Ulm, Germany; Institute of Surface Chemistry and Catalysis, Ulm University, 89081 Ulm, Germany;* orcid.org/0000 0002 7565 0628
Torsten Brezesinski − *Institute of Nanotechnology, Karlsruhe Institute of Technology (KIT), 76344 Eggenstein Leopoldshafen, Germany;* orcid.org/0000 0002 4336 263X

Complete contact information is available at: https://pubs.acs.org/10.1021/acs.chemmater.9b05285

Notes

The authors declare no competing financial interest.

■ ACKNOWLEDGMENTS

Financial support by the FET OPEN project "LiRichFCC" of the European Commission (grant agreement # 711792) is acknowledged. We would like to thank Dr. Edmund Welter and all staff from the Experiments Division XAS in PETRA III, Hamburg. A.A.G. and A.L.B. acknowledge the Grant of the Southern Federal University (VnGr 07/2017 08) for financial support. This work has been partially carried out with the support of the Karlsruhe Nano Micro Facility and contributes to the research performed at CELEST (Center for Electro chemical Energy Storage Ulm Karlsruhe).

■ REFERENCES

(1) Olivetti, E. A.; Ceder, G.; Gaustad, G. G.; Fu, X. Lithium Ion Battery Supply Chain Considerations: Analysis of Potential Bottle necks in Critical Metals. *Joule* **2017**, *1* (2), 229−243.
(2) Manthiram, A.; Knight, J. C.; Myung, S. T.; Oh, S. M.; Sun, Y. K. Nickel Rich and Lithium Rich Layered Oxide Cathodes: Progress and Perspectives. *Adv. Energy Mater.* **2016**, *6* (1), 1501010.
(3) Kim, J.; Lee, H.; Cha, H.; Yoon, M.; Park, M.; Cho, J. Prospect and Reality of Ni Rich Cathode for Commercialization. *Adv. Energy Mater.* **2018**, *8* (6), 1702028.
(4) Zheng, J.; Myeong, S.; Cho, W.; Yan, P.; Xiao, J.; Wang, C.; Cho, J.; Zhang, J. G. Li and Mn Rich Cathode Materials: Challenges to Commercialization. *Adv. Energy Mater.* **2017**, *7* (6), 1601284.
(5) Nitta, N.; Wu, F.; Lee, J. T.; Yushin, G. Li Ion Battery Materials: Present and Future. *Mater. Today* **2015**, *18* (5), 252−264.
(6) Bianchini, M.; Roca Ayats, M.; Hartmann, P.; Brezesinski, T.; Janek, J. There and Back Again The Journey of $LiNiO_2$ as a Cathode Active Material. *Angew. Chem., Int. Ed.* **2019**, *58* (31), 10434−10458.
(7) Thackeray, M. M.; Johnson, P. J.; de Picciotto, L. A.; Bruce, P. G.; Goodenough, J. B. Electrochemical Extraction of Lithium from $LiMn_2O_4$. *Mater. Res. Bull.* **1984**, *19* (2), 179−187.
(8) Liu, D.; Zhu, W.; Trottier, J.; Gagnon, C.; Barray, F.; Guerfi, A.; Mauger, A.; Groult, H.; Julien, C. M.; Goodenough, J. B.; Zaghib, K. Spinel Materials for High Voltage Cathodes in Li Ion Batteries. *RSC Adv.* **2014**, *4* (1), 154−167.
(9) Masquelier, C.; Croguennec, L. Polyanionic (Phosphates, Silicates, Sulfates) Frameworks as Electrode Materials for Recharge able Li (or Na) Batteries. *Chem. Rev.* **2013**, *113* (8), 6552−6591.
(10) Mather, G. C.; Dussarrat, C.; Etourneau, J.; West, A. R. A Review of Cation Ordered Rock Salt Superstructure Oxides. *J. Mater. Chem.* **2000**, *10* (10), 2219−2230.
(11) Xiao, J.; Chen, X.; Sushko, P. V.; Sushko, M. L.; Kovarik, L.; Feng, J.; Deng, Z.; Zheng, J.; Graff, G. L.; Nie, Z.; Choi, D.; Liu, J.; Zhang, J. G.; Whittingham, M. S. High Performance $LiNi_{0.5}Mn_{1.5}O_4$ Spinel Controlled by Mn^{3+} Concentration and Site Disorder. *Adv. Mater.* **2012**, *24* (16), 2109−2116.
(12) Zheng, J.; Xiao, J.; Yu, X.; Kovarik, L.; Gu, M.; Omenya, F.; Chen, X.; Yang, X. Q.; Liu, J.; Graff, G. L.; Whittingham, M. S.; Zhang, J. G. Enhanced Li^+Ion Transport in $LiNi_{0.5}Mn_{1.5}O_4$ through Control of Site Disorder. *Phys. Chem. Chem. Phys.* **2012**, *14* (39), 13515.
(13) Zeng, D.; Cabana, J.; Bréger, J.; Yoon, W. S.; Grey, C. P. Cation Ordering in $Li[Ni_xMn_xCo_{(1-2x)}]O_2$ Layered Cathode Materials: A Nuclear Magnetic Resonance (NMR), Pair Distribution Function, X Ray Absorption Spectroscopy, and Electrochemical Study. *Chem. Mater.* **2007**, *19* (25), 6277−6289.
(14) Armstrong, A. R.; Dupre, N.; Paterson, A. J.; Grey, C. P.; Bruce, P. G. Combined Neutron Diffraction, NMR, and Electrochemical Investigation of the Layered to Spinel Transformation in LiMnO2. *Chem. Mater.* **2004**, *16* (16), 3106−3118.
(15) Mitome, M.; Kohiki, S.; Murakawa, Y.; Hori, K.; Kurashima, K.; Bando, Y. Transmission Electron Microscopy and Electron Diffraction Study of the Short Range Ordering Structure of α $LiFeO_2$. *Acta Crystallogr., Sect. B: Struct. Sci.* **2004**, *60* (6), 698−704.
(16) Castellanos, M.; Martinez, M. C.; West, A. R. New Family of Phases, Li_2MXO_4: X = Zr, Hf; M = Mg, Mn, Fe, Co, Ni, Cu, Zn with α $LiFeO_2$ and Related Structures. *Z. Kristallogr.* **1990**, *190*, 161.
(17) Sakurai, Y.; Arai, H.; Okada, S.; Yamaki, J. Low Temperature Synthesis and Electrochemical Characteristics of $LiFeO_2$ Cathodes. *J. Power Sources* **1997**, *68* (2), 711−715.
(18) Chen, R.; Ren, S.; Knapp, M.; Wang, D.; Witter, R.; Fichtner, M.; Hahn, H. Disordered Lithium Rich Oxyfluoride as a Stable Host for Enhanced Li^+ Intercalation Storage. *Adv. Energy Mater.* **2015**, *5* (9), 1401814.
(19) Lee, J.; Urban, A.; Li, X.; Su, D.; Hautier, G.; Ceder, G. Unlocking the Potential of Cation Disordered Oxides for Recharge able Lithium Batteries. *Science,* **2014**, *343* (6170), 519−522.
(20) Yabuuchi, N.; Takeuchi, M.; Nakayama, M.; Shiiba, H.; Ogawa, M.; Nakayama, K.; Ohta, T.; Endo, D.; Ozaki, T.; Inamasu, T.; Sato, K.; Komaba, S. High Capacity Electrode Materials for Rechargeable Lithium Batteries: Li_3NbO_4 Based System with Cation Disordered Rocksalt Structure. *Proc. Natl. Acad. Sci.* **2015**, *112* (25), 7650−7655.
(21) Yabuuchi, N.; Nakayama, M.; Takeuchi, M.; Komaba, S.; Hashimoto, Y.; Mukai, T.; Shiiba, H.; Sato, K.; Kobayashi, Y.; Nakao, A.; Yonemura, M.; Yamanaka, K.; Mitsuhara, K.; Ohta, T. Origin of Stabilization and Destabilization in Solid State Redox Reaction of Oxide Ions for Lithium Ion Batteries. *Nat. Commun.* **2016**, *7* (1), 13814.
(22) Wang, X.; Huang, Y.; Ji, D.; Omenya, F.; Karki, K.; Sallis, S.; Piper, L. F. J.; Wiaderek, K. M.; Chapman, K. W.; Chernova, N. A.; Whittingham, M. S. Structure Evolution and Thermal Stability of High Energy Density Li Ion Battery Cathode Li_2VO_2F. *J. Electrochem. Soc.* **2017**, *164* (7), A1552−A1558.
(23) Dominko, R.; Garrido, C. V. A.; Bele, M.; Kuezma, M.; Arcon, I.; Gaberscek, M. Electrochemical Characteristics of $Li_{2-x}VTiO_4$ Rock Salt Phase in Li Ion Batteries. *J. Power Sources* **2011**, *196* (16), 6856−6862.
(24) Cambaz, M. A.; Vinayan, B. P.; Geßwein, H.; Schiele, A.; Sarapulova, A.; Diemant, T.; Mazilkin, A.; Brezesinski, T.; Behm, R. J.; Ehrenberg, H.; Fichtner, M. Oxygen Activity in Li Rich Disordered

Rock Salt Oxide and the Influence of $LiNbO_3$ Surface Modification on the Electrochemical Performance. *Chem. Mater.* **2019**, *31* (12), 4330−4340.
(25) Urban, A.; Abdellahi, A.; Dacek, S.; Artrith, N.; Ceder, G. Electronic Structure Origin of Cation Disorder in Transition Metal Oxides. *Phys. Rev. Lett.* **2017**, *119* (17), 176402.
(26) Cambaz, M. A.; Vinayan, B. P.; Pervez, S. A.; Johnsen, R. E.; Geßwein, H.; Guda, A. A.; Rusalev, Y. V.; Kinyanjui, M. K.; Kaiser, U.; Fichtner, M. Suppressing Dissolution of Vanadium from Cation Disordered $Li_{2\ x}VO_2F$ via a Concentrated Electrolyte Approach. *Chem. Mater.* **2019**, *31* (19), 7941−7950.
(27) Cambaz, M. A.; Vinayan, B. P.; Euchner, H.; Johnsen, R. E.; Guda, A. A.; Mazilkin, A.; Rusalev, Y. V.; Trigub, A. L.; Gross, A.; Fichtner, M. Design of Nickel Based Cation Disordered Rock Salt Oxides: The Effect of Transition Metal (M = V, Ti, Zr) Substitution in $LiNi_{0.5}M_{0.5}O_2$ Binary Systems. *ACS Appl. Mater. Interfaces* **2018**, *10* (26), 21957−21964.
(28) Cambaz, M. A.; Vinayan, B. P.; Euchner, H.; Pervez, S. A.; Geßwein, H.; Braun, T.; Gross, A.; Fichtner, M. Design and Tuning of the Electrochemical Properties of Vanadium Based Cation Disor dered Rock Salt Oxide Positive Electrode Material for Lithium Ion Batteries. *ACS Appl. Mater. Interfaces* **2019**, *11* (43), 39848−39858.
(29) Shigemura, H.; Tabuchi, M.; Sakaebe, H.; Kobayashi, H.; Kageyama, H. Lithium Extraction and Insertion Behavior of Nanocrystalline Li_2TiO_3 $LiFeO_2$ Solid Solution with Cubic Rock Salt Structure. *J. Electrochem. Soc.* **2003**, *150* (5), 638−644.
(30) Kitajou, A.; Tanaka, K.; Miki, H.; Koga, H.; Okajima, T.; Okada, S. Improvement of Cathode Properties by Lithium Excess in Disordered Rocksalt $Li_{2+2x}Mn_{1\ x}Ti_{1\ x}O_4$. *Electrochemistry* **2016**, *84* (8), 597−600.
(31) Twu, N.; Li, X.; Urban, A.; Balasubramanian, M.; Lee, J.; Liu, L.; Ceder, G. Designing New Lithium Excess Cathode Materials from Percolation Theory: Nanohighways in $Li_xNi_{2-4x/3}Sb_{x\ /3}O_2$. *Nano Lett.* **2015**, *15* (1), 596−602.
(32) Kan, W. H.; Wei, C.; Chen, D.; Bo, T.; Wang, B.; Zhang, Y.; Tian, Y.; Lee, J.; Liu, Y.; Chen, G. Evolution of Local Structural Ordering and Chemical Distribution upon Delithiation of a Rock Salt Structured $Li_{1.3}Ta_{0.3}Mn_{0.4}O_2$ Cathode. *Adv. Funct. Mater.* **2019**, *29* (17), 1808294.
(33) Lee, J.; Seo, D. H.; Balasubramanian, M.; Twu, N.; Li, X.; Ceder, G. A New Class of High Capacity Cation Disordered Oxides for Rechargeable Lithium Batteries: Li Ni Ti Mo Oxides. *Energy Environ. Sci.* **2015**, *8* (11), 3255−3265.
(34) Hoshino, S.; Glushenkov, A. M.; Ichikawa, S.; Ozaki, T.; Inamasu, T.; Yabuuchi, N. Reversible Three Electron Redox Reaction of Mo^{3+}/Mo^{6+} for Rechargeable Lithium Batteries. *ACS Energy Lett.* **2017**, *2* (4), 733−738.
(35) Jacquet, Q.; Iadecola, A.; Saubanère, M.; Li, H.; Berg, E. J.; Rousse, G.; Cabana, J.; Doublet, M. L.; Tarascon, J. M. Charge Transfer Band Gap as an Indicator of Hysteresis in Li Disordered Rock Salt Cathodes for Li Ion Batteries. *J. Am. Chem. Soc.* **2019**, *141* (29), 11452−11464.
(36) Zheng, S.; Dou, A.; Su, M.; Liu, Y. Influence of Nb Doping on Electrochemical Performance of Nanostructured Cation Disordered $Li_{1+x/100}Ni_{1/2\ x/100}Ti_{1/2\ x/100}Nb_{x/100}O_2$ Composites Cathode for Li Ion Batteries. *J. Nanosci. Nanotechnol.* **2020**, *20* (1), 452−459.
(37) Yu, Z.; Qu, X.; Dou, A.; Su, M.; Liu, Y.; Wu, F. Synthesis and Redox Mechanism of Cation Disordered, Rock Salt Cathode Material Li Ni Ti Nb O Compounds for a Li Ion Battery. *ACS Appl. Mater. Interfaces* **2019**, *11* (39), 35777−35787.
(38) Zheng, S.; Liu, D.; Tao, L.; Fan, X.; Liu, K.; Liang, G.; Dou, A.; Su, M.; Liu, Y.; Chu, D. Electrochemistry and Redox Characterization of Rock Salt Type Lithium Metal Oxides $Li_{1+z/3}Ni_{1/2\ z/2}Ti_{1/2+z/6}O_2$ for Li Ion Batteries. *J. Alloys Compd.* **2019**, *773*, 1−10.
(39) Sebastian, L.; Gopalakrishnan, J. Li_2MTiO_4 (M = Mn, Fe, Co, Ni): New Cation Disordered Rocksalt Oxides Exhibiting Oxidative Deintercalation of Lithium. Synthesis of an Ordered Li_2NiTiO_4. *J. Solid State Chem.* **2003**, *172* (1), 171−177.
(40) Zhao, E.; He, L.; Wang, B.; Li, X.; Zhang, J.; Wu, Y.; Chen, J.; Zhang, S.; Liang, T.; Chen, Y.; Yu, X.; Li, H.; Chen, L.; Huang, X.; Chen, H.; Wang, F. Structural and Mechanistic Revelations on High Capacity Cation Disordered Li Rich Oxides for Rechargeable Li Ion Batteries. *Energy Storage Mater.* **2019**, *16*, 354−363.
(41) Blasse, G. On the Structure of Some Compounds $Li_3Me^{5+}O_4$, and Some Other Mixed Metal Oxides Containing Lithium. *Z. Anorg. Allg. Chem.* **1964**, *331* (1−2), 44−50.
(42) Yabuuchi, N.; Tahara, Y.; Komaba, S.; Kitada, S.; Kajiya, Y. Synthesis and Electrochemical Properties of Li_4MoO_5 NiO Binary System as Positive Electrode Materials for Rechargeable Lithium Batteries. *Chem. Mater.* **2016**, *28* (2), 416−419.
(43) Nakajima, M.; Yabuuchi, N. Lithium Excess Cation Disordered Rocksalt Type Oxide with Nanoscale Phase Segregation: $Li_{1.25}Nb_{0.25}V_{0.5}O_2$. *Chem. Mater.* **2017**, *29* (16), 6927−6935.
(44) Momma, K.; Izumi, F. VESTA 3 for Three Dimensional Visualization of Crystal, Volumetric and Morphology Data. *J. Appl. Crystallogr.* **2011**, *44* (6), 1272−1276.
(45) Urban, A.; Lee, J.; Ceder, G. The Configurational Space of Rocksalt Type Oxides for High Capacity Lithium Battery Electrodes. *Adv. Energy Mater.* **2014**, *4* (13), 1400478.
(46) Lee, J.; Papp, J. K.; Clément, R. J.; Sallis, S.; Kwon, D. H.; Shi, T.; Yang, W.; McCloskey, B. D.; Ceder, G. Mitigating Oxygen Loss to Improve the Cycling Performance of High Capacity Cation Disordered Cathode Materials. *Nat. Commun.* **2017**, *8* (1), 981.
(47) Xu, K. Electrolytes and Interphases in Li Ion Batteries and Beyond. *Chem. Rev.* **2014**, *114* (23), 11503−11618.
(48) Aurbach, D.; Markovsky, B.; Salitra, G.; Markevich, E.; Talyossef, Y.; Koltypin, M.; Nazar, L.; Ellis, B.; Kovacheva, D. Review on Electrode Electrolyte Solution Interactions, Related to Cathode Materials for Li Ion Batteries. *J. Power Sources* **2007**, *165* (2), 491−499.
(49) Xu, B.; Fell, C. R.; Chi, M.; Meng, Y. S. Identifying Surface Structural Changes in Layered Li Excess Nickel Manganese Oxides in High Voltage Lithium Ion Batteries: A Joint Experimental and Theoretical Study. *Energy Environ. Sci.* **2011**, *4* (6), 2223.
(50) Metzger, M.; Strehle, B.; Solchenbach, S.; Gasteiger, H. A. Origin of H_2 Evolution in LIBs: H_2O Reduction vs. Electrolyte Oxidation. *J. Electrochem. Soc.* **2016**, *163* (5), A798−A809.
(51) Berkes, B. B.; Schiele, A.; Sommer, H.; Brezesinski, T.; Janek, J. On the Gassing Behavior of Lithium Ion Batteries with NCM523 Cathodes. *J. Solid State Electrochem.* **2016**, *20* (11), 2961−2967.
(52) Renfrew, S. E.; McCloskey, B. D. Residual Lithium Carbonate Predominantly Accounts for First Cycle CO_2 and CO Outgassing of Li Stoichiometric and Li Rich Layered Transition Metal Oxides. *J. Am. Chem. Soc.* **2017**, *139* (49), 17853−17860.
(53) Hatsukade, T.; Schiele, A.; Hartmann, P.; Brezesinski, T.; Janek, J. Origin of Carbon Dioxide Evolved during Cycling of Nickel Rich Layered NCM Cathodes. *ACS Appl. Mater. Interfaces* **2018**, *10* (45), 38892−38899.
(54) Qian, D.; Xu, B.; Chi, M.; Meng, Y. S. Uncovering the Roles of Oxygen Vacancies in Cation Migration in Lithium Excess Layered Oxides. *Phys. Chem. Chem. Phys.* **2014**, *16* (28), 14665−14668.
(55) Castel, E.; Berg, E. J.; El Kazzi, M.; Novák, P.; Villevieille, C. Differential Electrochemical Mass Spectrometry Study of the Interface of $xLi_2MnO_3\cdot(1\ x)LiMO_2$ (M = Ni, Co, and Mn) Material as a Positive Electrode in Li Ion Batteries. *Chem. Mater.* **2014**, *26* (17), 5051−5057.
(56) Hong, J.; Lim, H. D.; Lee, M.; Kim, S. W.; Kim, H.; Oh, S. T.; Chung, G. C.; Kang, K. Critical Role of Oxygen Evolved from Layered Li Excess Metal Oxides in Lithium Rechargeable Batteries. *Chem. Mater.* **2012**, *24* (14), 2692−2697.
(57) Shannon, B. Y. R. D.; H, M.; Baur, N. H.; Gibbs, O. H.; Eu, M.; Cu, V.; Shannon, R. D. Revised Effective Ionic Radii and Systematic Studies of Interatomic Distances in Halides and Chalcogenides. *Acta Crystallogr., Sect. A: Cryst. Phys., Diffr., Theor. Gen. Crystallogr.* **1976**, *32* (5), 751−767.
(58) Sathiya, M.; Rousse, G.; Ramesha, K.; Laisa, C. P.; Vezin, H.; Sougrati, M. T.; Doublet, M. L.; Foix, D.; Gonbeau, D.; Walker, W.;

Prakash, A. S.; Ben Hassine, M.; Dupont, L.; Tarascon, J. M. Reversible Anionic Redox Chemistry in High Capacity Layered Oxide Electrodes. *Nat. Mater.* **2013**, *12* (9), 827−835.
(59) Rougier, A.; Delmas, C.; Chadwick, A. V. Non Cooperative Jahn Teller Effect in $LiNiO_2$: An EXAFS Study. *Solid State Commun.* **1995**, *94* (2), 123−127.
(60) Deb, A.; Bergmann, U.; Cramer, S. P.; Cairns, E. J. Local Structure of $LiNi_{0.5}Mn_{0.5}O_2$ Cathode Material Probed by in Situ X Ray Absorption Spectroscopy. *J. Appl. Phys.* **2006**, *99* (6), 063701.
(61) Rehr, J. J.; Stern, E. A.; Martin, R. L.; Davidson, E. R. Extended X Ray Absorption Fine Structure Amplitudes—Wave Function Relaxation and Chemical Effects. *Phys. Rev. B: Condens. Matter Mater. Phys.* **1978**, *17* (2), 560−565.
(62) Stern, E. A.; Bunker, B. A.; Heald, S. M. Many Body Effects on Extended X Ray Absorption Fine Structure Amplitudes. *Phys. Rev. B: Condens. Matter Mater. Phys.* **1980**, *21* (12), 5521−5539.
(63) Abdellahi, A.; Urban, A.; Dacek, S.; Ceder, G. The Effect of Cation Disorder on the Average Li Intercalation Voltage of Transition Metal Oxides. *Chem. Mater.* **2016**, *28* (11), 3659−3665.
(64) Jayarathne, U.; Chandrasekaran, P.; Greene, A. F.; Mague, J. T.; DeBeer, S.; Lancaster, K. M.; Sproules, S.; Donahue, J. P. X Ray Absorption Spectroscopy Systematics at the Tungsten L Edge. *Inorg. Chem.* **2014**, *53* (16), 8230−8241.
(65) Subías, G.; Blasco, J.; García, J.; Herrero Martín, J.; Sánchez, M. C. Order Disorder Nature of the Antiferroelectric Transition in Pb_2MnWO_6. *J. Phys.: Condens. Matter* **2009**, *21* (7), 075903.
(66) Yamazoe, S.; Hitomi, Y.; Shishido, T.; Tanaka, T. XAFS Study of Tungsten L_1 and L_3 Edges: Structural Analysis of WO_3 Species Loaded on TiO_2 as a Catalyst for Photo Oxidation of NH_3. *J. Phys. Chem. C* **2008**, *112* (17), 6869−6879.
(67) Edström, K.; Gustafsson, T.; Thomas, J. O. The Cathode Electrolyte Interface in the Li Ion Battery. *Electrochim. Acta* **2004**, *50* (2−3), 397−403.
(68) Croy, J. R.; Balasubramanian, M.; Gallagher, K. G.; Burrell, A. K. Review of the U.S. Department of Energy's "Deep Dive" Effort to Understand Voltage Fade in Li and Mn Rich Cathodes. *Acc. Chem. Res.* **2015**, *48* (11), 2813−2821.
(69) Tran, N.; Croguennec, L.; Ménétrier, M.; Weill, F.; Biensan, P.; Jordy, C.; Delmas, C. Mechanisms Associated with the "Plateau" Observed at High Voltage for the Overlithiated $Li_{1.12}(Ni_{0.425}Mn_{0.425}Co_{0.15})_{0.88}O_2$ System. *Chem. Mater.* **2008**, *20* (15), 4815−4825.
(70) Rozier, P.; Tarascon, J. M. Review—Li Rich Layered Oxide Cathodes for Next Generation Li Ion Batteries: Chances and Challenges. *J. Electrochem. Soc.* **2015**, *162* (14), 2490−2499.
(71) Assat, G.; Tarascon, J. M. Fundamental Understanding and Practical Challenges of Anionic Redox Activity in Li Ion Batteries. *Nat. Energy* **2018**, *3* (5), 373−386.
(72) Chen, D.; Kan, W. H.; Chen, G. Understanding Performance Degradation in Cation Disordered Rock Salt Oxide Cathodes. *Adv. Energy Mater.* **2019**, *9* (31), 1901255.
(73) Saubanère, M.; McCalla, E.; Tarascon, J. M. M.; Doublet, M. L. L. The Intriguing Question of Anionic Redox in High Energy Density Cathodes for Li Ion Batteries. *Energy Environ. Sci.* **2016**, *9* (3), 984−991.
(74) Taylor, Z. N.; Perez, A. J.; Coca Clemente, J. A.; Braga, F.; Drewett, N. E.; Pitcher, M. J.; Thomas, W. J.; Dyer, M. S.; Collins, C.; Zanella, M.; Johnson, T.; Day, S.; Tang, C.; Dhanak, V. R.; Claridge, J. B.; Hardwick, L. J.; Rosseinsky, M. J. Stabilization of O O Bonds by D^0 Cations in $Li_{4+x}Ni_{1-x}WO_6$ ($0 \leq x \leq 0.25$) Rock Salt Oxides as the Origin of Large Voltage Hysteresis. *J. Am. Chem. Soc.* **2019**, *141* (18), 7333−7346.
(75) Maitra, U.; House, R. A.; Somerville, J. W.; Tapia Ruiz, N.; Lozano, J. G.; Guerrini, N.; Hao, R.; Luo, K.; Jin, L.; Pérez Osorio, M. A.; Massel, F.; Pickup, D. M.; Ramos, S.; Lu, X.; McNally, D. E.; Chadwick, A. V.; Giustino, F.; Schmitt, T.; Duda, L. C.; Roberts, M. R.; Bruce, P. G. Oxygen Redox Chemistry without Excess Alkali Metal Ions in $Na_{2/3}[Mg_{0.28}Mn_{0.72}]O_2$. *Nat. Chem.* **2018**, *10* (3), 288−295.
(76) House, R. A.; Maitra, U.; Jin, L.; Lozano, J. G.; Somerville, J. W.; Rees, N. H.; Naylor, A. J.; Duda, L. C.; Massel, F.; Chadwick, A. V.; Ramos, S.; Pickup, D. M.; McNally, D. E.; Lu, X.; Schmitt, T.; Roberts, M. R.; Bruce, P. G. What Triggers Oxygen Loss in Oxygen Redox Cathode Materials? *Chem. Mater.* **2019**, *31* (9), 3293−3300.
(77) Croy, J. R.; Gallagher, K. G.; Balasubramanian, M.; Chen, Z.; Ren, Y.; Kim, D.; Kang, S. H.; Dees, D. W.; Thackeray, M. M. Examining Hysteresis in Composite $xLi_2MnO_3 \cdot (1-x)LiMO_2$ Cathode Structures. *J. Phys. Chem. C* **2013**, *117* (13), 6525−6536.
(78) Gent, W. E.; Lim, K.; Liang, Y.; Li, Q.; Barnes, T.; Ahn, S. J.; Stone, K. H.; McIntire, M.; Hong, J.; Song, J. H.; Li, Y.; Mehta, A.; Ermon, S.; Tyliszczak, T.; Kilcoyne, D.; Vine, D.; Park, J. H.; Doo, S. K.; Toney, M. F.; Yang, W.; Prendergast, D.; Chueh, W. C. Coupling between Oxygen Redox and Cation Migration Explains Unusual Electrochemistry in Lithium Rich Layered Oxides. *Nat. Commun.* **2017**, *8* (1), 2091.
(79) House, R. A.; Maitra, U.; Pérez Osorio, M. A.; Lozano, J. G.; Jin, L.; Somerville, J. W.; Duda, L. C.; Nag, A.; Walters, A.; Zhou, K. J.; Roberts, M. R.; Bruce, P. G. Superstructure Control of First Cycle Voltage Hysteresis in Oxygen Redox Cathodes. *Nature* **2020**, *577* (7791), 502−508.
(80) Mortemard de Boisse, B.; Nishimura, S.; Watanabe, E.; Lander, L.; Tsuchimoto, A.; Kikkawa, J.; Kobayashi, E.; Asakura, D.; Okubo, M.; Yamada, A. Highly Reversible Oxygen Redox Chemistry at 4.1 V in $Na_{4/7-x}[\square_{1/7}Mn_{6/7}]O_2$ ($\square$:Mn Vacancy). *Adv. Energy Mater.* **2018**, *8* (20), 1800409.
(81) Song, B.; Tang, M.; Hu, E.; Borkiewicz, O. J.; Wiaderek, K. M.; Zhang, Y.; Phillip, N. D.; Liu, X.; Shadike, Z.; Li, C.; Song, L.; Hu, Y. Y.; Chi, M.; Veith, G. M.; Yang, X. Q.; Liu, J.; Nanda, J.; Page, K.; Huq, A. Understanding the Low Voltage Hysteresis of Anionic Redox in $Na_2Mn_3O_7$. *Chem. Mater.* **2019**, *31* (10), 3756−3765.
(82) Kresse, G.; Furthmüller, J. Efficient Iterative Schemes for Ab Initio Total Energy Calculations Using a Plane Wave Basis Set. *Phys. Rev. B: Condens. Matter Mater. Phys.* **1996**, *54* (16), 11169−11186.
(83) Kresse, G.; Furthmüller, J. Efficiency of Ab Initio Total Energy Calculations for Metals and Semiconductors Using a Plane Wave Basis Set. *Comput. Mater. Sci.* **1996**, *6* (1), 15−50.
(84) Blöchl, P. E. Projector Augmented Wave Method. *Phys. Rev. B: Condens. Matter Mater. Phys.* **1994**, *50* (24), 17953−17979.
(85) Hart, G. L. W.; Forcade, R. W. Generating Derivative Structures from Multilattices: Algorithm and Application to Hcp Alloys. *Phys. Rev. B: Condens. Matter Mater. Phys.* **2009**, *80* (1), 014120.
(86) Hart, G. L. W.; Nelson, L. J.; Forcade, R. W. Generating Derivative Structures at a Fixed Concentration. *Comput. Mater. Sci.* **2012**, *59*, 101−107.
(87) Ong, S. P.; Richards, W. D.; Jain, A.; Hautier, G.; Kocher, M.; Cholia, S.; Gunter, D.; Chevrier, V. L.; Persson, K. A.; Ceder, G. Python Materials Genomics (Pymatgen): A Robust, Open Source Python Library for Materials Analysis. *Comput. Mater. Sci.* **2013**, *68*, 314−319.
(88) Perdew, J. P.; Burke, K.; Ernzerhof, M. Generalized Gradient Approximation Made Simple. *Phys. Rev. Lett.* **1996**, *77* (18), 3865−3868.
(89) Dudarev, S. L.; Botton, G. A.; Savrasov, S. Y.; Humphreys, C. J.; Sutton, A. P. Electron Energy Loss Spectra and the Structural Stability of Nickel Oxide: An LSDA+U Study. *Phys. Rev. B: Condens. Matter Mater. Phys.* **1998**, *57* (3), 1505−1509.
(90) Anisimov, V. I.; Zaanen, J.; Andersen, O. K. Band Theory and Mott Insulators: Hubbard U Instead of Stoner I. *Phys. Rev. B: Condens. Matter Mater. Phys.* **1991**, *44* (3), 943−954.
(91) Jain, A.; Hautier, G.; Moore, C. J.; Ping Ong, S.; Fischer, C. C.; Mueller, T.; Persson, K. A.; Ceder, G. A High Throughput Infrastructure for Density Functional Theory Calculations. *Comput. Mater. Sci.* **2011**, *50* (8), 2295−2310.
(92) Sun, J.; Remsing, R. C.; Zhang, Y.; Sun, Z.; Ruzsinszky, A.; Peng, H.; Yang, Z.; Paul, A.; Waghmare, U.; Wu, X.; Klein, M. L.; Perdew, J. P. Accurate First Principles Structures and Energies of Diversely Bonded Systems from an Efficient Density Functional. *Nat. Chem.* **2016**, *8* (9), 831−836.

(93) Sai Gautam, G.; Carter, E. A. Evaluating Transition Metal Oxides within DFT SCAN and SCAN+U Frameworks for Solar Thermochemical Applications. *Phys. Rev. Mater.* **2018**, *2* (9), 095401.
(94) Urban, A.; Seo, D. H. H.; Ceder, G. Computational Understanding of Li Ion Batteries. *npj Comput. Mater.* **2016**, *2* (1), 16002.
(95) Aydinol, M. K.; Kohan, A. F.; Ceder, G.; Cho, K.; Joannopoulos, J. Ab Initio Study of Lithium Intercalation in Metal Oxides and Metal Dichalcogenides. *Phys. Rev. B: Condens. Matter Mater. Phys.* **1997**, *56* (3), 1354−1365.
(96) Berkes, B. B.; Jozwiuk, A.; Vračar, M.; Sommer, H.; Brezesinski, T.; Janek, J. Online Continuous Flow Differential Electrochemical Mass Spectrometry with a Realistic Battery Setup for High Precision, Long Term Cycling Tests. *Anal. Chem.* **2015**, *87* (12), 5878−5883.
(97) Ravel, B.; Newville, M. ATHENA, ARTEMIS, HEPHAESTUS: Data Analysis for X Ray Absorption Spectroscopy Using IFEFFIT. *J. Synchrotron Radiat.* **2005**, *12* (4), 537−541.
(98) Zabinsky, S. I.; Rehr, J. J.; Ankudinov, A.; Albers, R. C.; Eller, M. J. Multiple Scattering Calculations of X Ray Absorption Spectra. *Phys. Rev. B: Condens. Matter Mater. Phys.* **1995**, *52* (4), 2995−3009.
(99) Ashiotis, G.; Deschildre, A.; Nawaz, Z.; Wright, J. P.; Karkoulis, D.; Picca, F. E.; Kieffer, J. The Fast Azimuthal Integration Python Library: PyFAI. *J. Appl. Crystallogr.* **2015**, *48* (2), 510−519.